Dependence of Differential Mixing on N and R_ρ

WILLIAM J. MERRYFIELD

Canadian Centre for Climate Modelling and Analysis, Meteorological Service of Canada, Victoria, British Columbia, Canada

(Manuscript received 7 June 2004, in final form 23 December 2004)

ABSTRACT

Mechanisms and parameter dependence of differential mixing of heat and salt by ocean turbulence are investigated numerically by extending a previous study to examine dependence upon buoyancy frequency N and density gradient ratio R_ρ. In these experiments a burst of turbulence mixes temperature T and pseudosalinity S having molecular diffusivity 0.1 times that of T across background vertical gradients of both quantities. In contrast to previous results, which found turbulent diffusivity ratios $d = K_S/K_T < 1$ at a fixed N, the present study finds that $d > 1$ when $N = 0$ and that d tends to approach this value as $N \to 0$. In all cases considered, d is larger at high R_ρ (buoyancy dominated by T) than at low R_ρ (buoyancy dominated by S). It is shown that this tendency is consistent with differential mixing being largely due to preferential restratification of the slower-diffusing component S. This conclusion is reinforced by the finding that d scales linearly with a fractional restratification measure over a wide range of conditions.

1. Introduction

A number of recent studies have focused on whether weak intermittent turbulence, as prevails throughout much of the ocean interior, mixes heat and salt unequally when the large-scale vertical gradients of both components are stabilizing so that double diffusion is not active. This is a question of obvious relevance to the parameterization of turbulence in ocean models (Gargett and Holloway 1992; Merryfield et al. 1999). Several lines of evidence point toward the turbulent diffusivity K_T of heat, the more microscopically diffusive component, exceeding that of salt (K_S) when turbulence is sufficiently weak so that $d = K_S/K_T < 1$. Such a relation has been found in laboratory experiments (Turner 1968; Altman and Gargett 1990; Hebert and Ruddick 2003; Jackson and Rehmann 2003) and in direct numerical simulations (DNS) (Merryfield et al. 1998; Gargett et al. 2003; Smyth et al. 2005, this issue) and is suggested by the few simultaneous measurements of oceanic temperature and salinity microstructure so far undertaken (Nash and Moum 2002). These results and some possible observational consequences of differential mixing are summarized by Gargett (2003).

The DNS study of Gargett et al. (2003; henceforth GMH) examined differential mixing in a three-dimensional fluid stratified by stabilizing gradients of temperature T and a pseudosalinity S whose molecular diffusivity is ten times smaller than that of T. The intermittent nature of turbulence in the ocean was accounted for by considering mixing due to a turbulent burst whose specified initial velocities are sufficient to overturn the initially undisturbed stratification. The resulting decaying, stratified turbulence was shown to produce microstructure signatures similar to those measured in the ocean and led to preferential mixing of T as described above. This effect was argued to be due largely to preferential restratification of S.

The computations of GMH examined mainly the dependence of differential mixing on initial turbulent kinetic energy. The ratio d was found to be considerably less than 1 when turbulence is weak and to increase toward 1 as turbulence becomes more energetic, in broad agreement with laboratory results of Altman and Gargett (1990), Hebert and Ruddick (2003; henceforth HR) and Jackson and Rehmann (2003; henceforth JR). However, in the computations of GMH the intensity of turbulence relative to the stabilizing influence of stratification was limited to buoyancy Reynolds numbers $\varepsilon/\nu N^2 \lesssim 10^3$, where ε is the rate of kinetic energy dissipation, ν is molecular viscosity, and N is buoyancy frequency, whereas JR considered $\varepsilon/\nu N^2$ of at least an order of magnitude larger. In addition, GMH considered only cases in which T and S contribute equally to density stratification, whereas JR and HR consider instances in which stratification is dominated by either the slower- or faster-diffusing component.

The aims of the present paper are thus twofold. First, the GMH study is extended to values of $\varepsilon/\nu N^2$ as large

Corresponding author address: Dr. William Merryfield, Canadian Centre for Climate Modelling and Analysis, University of Victoria, P.O. Box 1700, Victoria, BC V8W 2Y2, Canada.
E-mail: bill.merryfield@ec.gc.ca

as those considered by JR. Of particular interest in this regard is an apparent transition, seen in the results of both JR and of HR, from $d < 1$ to $d > 1$ at large $\varepsilon/\nu N^2$. Because it is not computationally feasible to further increase the kinetic energy of the turbulence and hence ε in the DNS, this extension is accomplished instead by reducing N. (The extreme case of differential mixing in unstratified turbulence, i.e., $N = 0$, is also considered.) A gross equivalence between these two means of adjusting $\varepsilon/\nu N^2$ can be argued if this quantity is interpreted as the squared ratio of the buoyancy time scale N^{-1} and the turnover time scale $(\nu/\varepsilon)^{1/2}$ characterizing dissipation-scale eddies, which governs that rate at which scalar gradients are amplified and hence the rate of turbulent mixing (Batchelor 1959). Increasing $\varepsilon/\nu N^2$ whether by increasing ε or decreasing N leads to more complete mixing prior to the time at which buoyancy can strongly influence the flow. Thus, increasing $(\nu/\varepsilon)^{1/2}$ in each case diminishes restratification, and hence (as argued below) the potential for differential mixing.

The second aim of this paper is to examine the dependence of differential diffusion on the relative contributions of T and S to the buoyancy, and hence on the density gradient ratio $R_\rho = \alpha\overline{T}_z/(-\beta\overline{S}_z)$, where $\alpha = -\rho^{-1}(\partial\rho/\partial T)_{S,p}$ is the thermal expansion coefficient, $\beta = \rho^{-1}(\partial\rho/\partial S)_{T,p}$ is the saline contraction coefficient, p is pressure, ρ is density, and $\overline{T}_z$ and $\overline{S}_z$ are the vertical T and S gradients of the undisturbed stratification. Whereas GMH considered exclusively $R_\rho = 1$, R_ρ will be varied here over its maximum range by considering extreme cases where T is passive and buoyancy is due entirely to S ($R_\rho = 0$), and where S is passive and buoyancy is due entirely to T ($R_\rho = \infty$). These computations will be compared with experiments at differing R_ρ reported by JR and HR and with closure-theory-based predictions of Canuto et al. (2002).

The setup of the numerical experiments and the numerical method and parameter values considered are described in section 2. Results are reported in section 3 and are interpreted in section 4 with particular attention to the hypothesized role of restratification. In section 5 these findings are related to the experimental and theoretical results mentioned above, and conclusions are presented in section 6.

2. Numerical experiments

The experimental setup and numerical method, described in detail in GMH, are reviewed briefly here. The equations considered are the Boussinesq equations describing motion in a medium stratified by T and S,

$$\frac{\partial \mathbf{u}}{\partial t} + (\mathbf{u}\cdot\boldsymbol{\nabla})\mathbf{u} = -\frac{1}{\rho_0}\boldsymbol{\nabla}p + \frac{\rho}{\rho_0}\mathbf{g} + \nu\nabla^2\mathbf{u}, \tag{1}$$

$$\boldsymbol{\nabla}\cdot\mathbf{u} = 0, \tag{2}$$

$$\frac{\partial T}{\partial t} + (\mathbf{u}\cdot\boldsymbol{\nabla})T = \kappa_T\nabla^2 T, \quad \text{and} \tag{3}$$

$$\frac{\partial S}{\partial t} + (\mathbf{u}\cdot\boldsymbol{\nabla})S = \kappa_S\nabla^2 S, \tag{4}$$

and a linear equation of state,

$$\rho = \rho_0[1 - \alpha(T - T_0) + \beta(S - S_0)], \tag{5}$$

where κ_T and κ_S are the microscopic coefficients of thermal and saline diffusion, ρ is density, $\mathbf{g}$ is gravitational acceleration, and ρ_0, T_0, and S_0 are constant reference values. Velocity $\mathbf{u}$ is represented as the sum of toroidal, poloidal, and horizontal mean components so that pressure p is eliminated, and the incompressibility condition (2) is satisfied exactly. This leads to four nonlinear equations for three-dimensional scalar fields and one for a one-dimensional vector field, given by the GMH Eqs. (12)–(16), which are solved pseudospectrally for a cubic, triply periodic domain. Advection terms are advanced in time using a Robert-filtered leapfrog scheme, and diffusive terms are represented by exponential integration factors.

The nondimensionalized[1] governing equations contain three dimensionless parameters: the Prandtl number $\sigma = \nu/\kappa_T$, the inverse Lewis number $\tau = \kappa_S/\kappa_T$, and R_ρ. Following GMH, $\sigma = 7$, representative of seawater, is chosen but, whereas $\tau \approx 0.01$ in seawater, $\tau = 0.1$ is chosen instead to narrow the range of spatial scales that must be resolved and to render the computation more tractable. As a result, these experiments, like those of GMH, will tend to underestimate effects of differential mixing, assuming such effects become increasingly pronounced as $\tau \to 0$. This limitation is partially overcome by additionally computing the paths of a large number of Lagrangian particles, which enables the transport of a nondiffusive ($\tau = 0$) passive tracer to be computed as described in section 4.

Initial conditions consist of a specified velocity field, concentrated at the gravest mode and energetic enough to cause overturning. Whereas GMH varied the magnitude and functional form of this velocity field, this study will, in addition, explore the influence of stratification on differential mixing by varying the buoyancy frequency, $N = [-g\partial_z(-\alpha\overline{T}_z + \beta\overline{S}_z)]^{1/2}$, and density gradient ratio $R_\rho = \alpha\overline{T}_z/(-\beta\overline{S}_z)$. This parameter space can be represented as an $\alpha\overline{T}_z$ versus $\beta\overline{S}_z$ plane as in Fig. 1, where the diagonal dashed lines describe contours of constant N and the thin solid lines contours of constant R_ρ. Experiments of GMH, taken as central cases here, are denoted by the black square at $N = N_0$, $R_\rho = 1$.

[1] As in GMH, length is dimensional by δ, time by κ_T/δ^2, and the T and S by $\overline{T}_z\delta$ and $\overline{S}_z\delta$, where $\delta \equiv (g\alpha\overline{T}_z/\kappa_T\nu)^{-1/4}$. For stratification and physical parameters typical of the upper-midlatitude thermocline, the dimensional width of the computational domain is about 17 cm, and the default buoyancy frequency is $N_0 \approx 6 \times 10^{-3}\ \mathrm{s}^{-1}$.

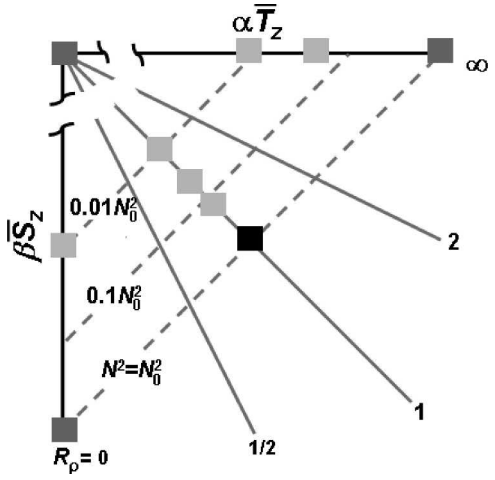

FIG. 1. Values of N and R_ρ considered in the DNS. The black square represents the central cases considered by Gargett et al. (2003), the darkly shaded squares are the primary sensitivity experiments (unstratified at origin, S-passive on horizontal axis, T-passive on vertical axis), and the lightly shaded squares are ancillary experiments at intermediate N.

Three principal sensitivity experiments are denoted by the darkly shaded squares: (i) an unstratified case with $N = 0$, (ii) a T-passive case with $N = N_0$ and $R_\rho = 0$, and (iii) an S-passive case with $N = N_0$ and $R_\rho = \infty$. In addition, various ancillary experiments in which N lies between 0 and N_0 are denoted by lightly shaded squares.[2] These values of (N, R_ρ) are considered for each of three values of initial kinetic energy E_0; the low-E_0, medium-E_0, and high-E_0 cases correspond, when $N = N_0$ and $R_\rho = 1$, to GMH experiments A3.0, A4.0, and A4.5. In addition, a medium-E_0 case with $\sigma = 2$ is included to illustrate sensitivity to Prandtl number. The experimental parameters are summarized in Tables 1 and 2.

Several measures are taken to speed the computations. As in GMH, higher spatial resolution is assigned to less diffusive S in the high-E_0 runs (Table 1); adequacy of these spatial resolutions is demonstrated in appendix A of GMH. Because of the rundown nature of the experiments, the computations in this study were stopped and restarted every 500 time steps to take advantage of the relaxation of the CFL time step constraint as the turbulent velocities decay. Comparison of the central A4.5 run with the corresponding GMH run, for which restarts were performed much less frequently, indicates that this procedure does not significantly affect the computed turbulent fluxes. In the end stages of the A4.5 runs, fields were Fourier interpolated to a $(32)^3$ grid once virtually all variance on finer scales had decayed away, and the runs were concluded using this coarser resolution. This was especially helpful for the low-N runs, which exhibited slow but significant evolution at times $\gg 2\pi/N_0$.

[2] Variation of N and R_ρ is achieved by adjusting the coefficient in (5) while retaining unit values for dimensionless $\overline{T}_z$ and $\overline{S}_z$.

TABLE 1. Properties of central runs. Initial Reynolds number $\mathrm{Re}_0 \equiv U_0 L_o/\sigma$ and Froude number $\mathrm{Fr}_0 \equiv U_0/NL_0$ are computed using eddy scales $U_0 = (2E_0)^{1/2}$ and $L_0 = (E_0/Z_0)^{1/2}$, where $E_0 = (1/2)\int|\mathbf{u}_0|^2\, d\mathbf{x}$ is initial kinetic energy and $Z_0 = (1/2)\int|\nabla \times \mathbf{u}_0|^2\, d\mathbf{x}$ is initial enstrophy.

Run	T resolution*	S resolution*	E_0	σ	Re_0	Fr_0
A3.0	$(64)^3$	$(64)^3$	10^3	7	10	4
A4.0	$(64)^3$	$(64)^3$**	10^4	7	31	12
A4.5	$(128)^3$	$(256)^3$	$10^{4.5}$	7	56	22
A4.0Pr2	$(64)^3$	$(64)^3$	10^4	2	31	12

* Collocation points in x, y, and z.
** Turbulent fluxes with $(128)^3$ resolution in S are nearly identical to those at this resolution.

TABLE 2. Values of N and R_ρ in DNS experiments.

Runs	N^2/N_0^2	R_ρ	Type
Central	1	1	
Primary	0	1	Unstratified
	1	0	T passive
	1	∞	S passive
Ancillary	0.2	1	
	0.05	1	
	0.01	1	
	0.01	0	T passive
	0.05	∞	S passive
	0.01	∞	S passive

3. Results

Measured values of turbulent diffusivity ratio d for each of the DNS runs, computed as

$$d = \int_0^{t_{\max}} \langle wS' \rangle\, dt \Big/ \int_0^{t_{\max}} \langle wT' \rangle\, dt, \tag{6}$$

where w is vertical velocity and the primes denote departures from background T and S and the angle brackets denote spatial averages, are shown[3] in Fig. 2. Several general trends are evident:

1) for each unstratified run, $d > 1$, whereas generally $d < 1$ for the stratified runs;
2) at fixed R_ρ, d generally increases toward $N = 0$ values as N becomes smaller;
3) at fixed N, d is smaller when T is passive ($R_\rho = 0$) than when S is passive ($R_\rho = \infty$)—at $R_\rho = 1$, d lies between these values;

[3] Because background T and S gradients have unit values under the nondimensional scaling employed, $d = K_S/K_T$. This is the inverse of the cumulative flux ratio f reported in GMH, and is considered to aid comparison with other investigations in section 5.

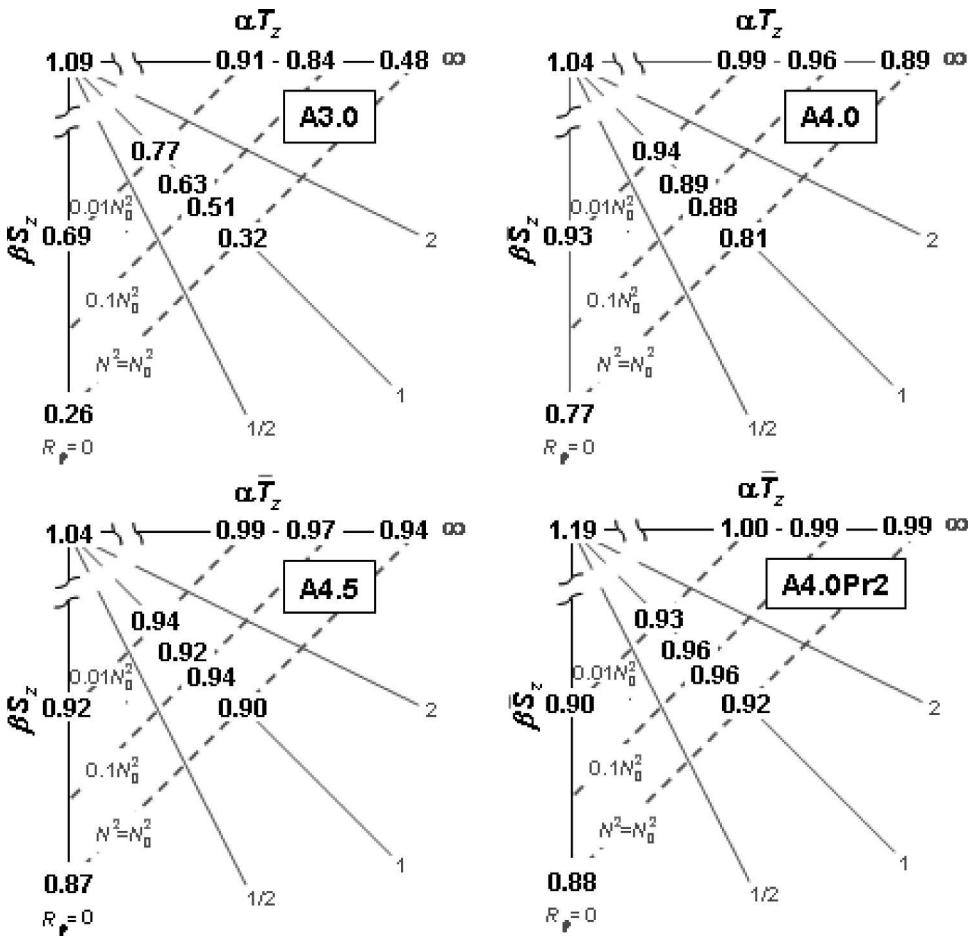

FIG. 2. Values of the turbulent diffusivity ratio, $d = K_S/K_T$, for all DNS runs.

4) at fixed N and R_ρ, d generally grows nearer to 1 as the intensity of mixing (i.e., E_0) increases; and
5) at fixed N, R_ρ, and E_0, d is generally larger at Prandtl number $\sigma = 2$ than at the more realistic value $\sigma = 7$.

Before interpreting these tendencies in the next section, it should be noted that the values for d shown in Fig. 2 are limits realized at sufficiently large $t_{\max}$. For low-N runs especially, $t_{\max}$ beyond which d no longer evolves significantly can be quite large due to the very long buoyancy time scale. This is illustrated by Fig. 3, which shows d as a function of $t_{\max}$ for each of the A4.5, $R_\rho = 1$ runs. In each instance for which $N > 0$, convergence is achieved after roughly four buoyancy periods $2\pi/N$. In the case with $N^2/N_0^2 = 0.01$, for example, this is approximately 40 times the default buoyancy period $2\pi/N_0$.

4. Interpretation: The role of restratification

In GMH, it was argued that the apparent tendency for K_T to exceed K_S in stratified turbulence is the result of countergradient (i.e., restratifying) transport of S exceeding that of T, and hence preferentially reversing the initial downgradient transport of S. This viewpoint is adopted in the following discussion and is shown to be qualitatively consistent with the tendencies described in section 3.

a. Dependence on N

Differences between the cases with default stratification ($N = N_0$, $d < 1$) and the unstratified cases ($N = 0$, $d > 1$) are first considered. As pointed out by GMH, during the initial stages of a stratified mixing event, overall transport of both T and S is downgradient and is accomplished by fluid elements moving (on average) away from their level of origin; T' and S' are anticorrelated with w, and $K_T \equiv -\langle wT' \rangle / \bar{T}_z$ and $K_S \equiv -\langle wS' \rangle / \bar{S}_z$ are both positive. Because anomalies of S diffuse away less rapidly than anomalies of T, downgradient transport of S is more efficient than that of T so that $K_S > K_T$ during this phase.

After turbulent velocities have decayed sufficiently that the negative buoyancy of displaced fluid particles outweighs inertial effects, fluid elements begin system-

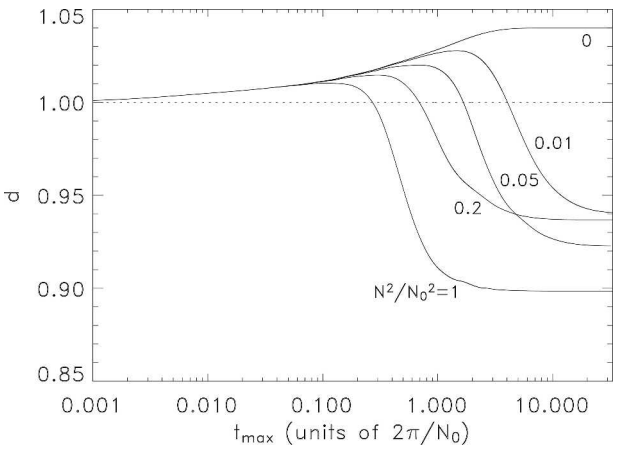

FIG. 3. Turbulent diffusivity ratio d, based on advective fluxes integrated from $t = 0$ to $t = t_{max}$ as in Eq. (6), for A4.5 runs with $R_\rho = 1$.

atically to return toward their levels of origin, that is, to restratify. During this phase, positive S' and negative T' will tend to be correlated with downward w so that $\langle wS' \rangle$ and $\langle wT' \rangle$ have opposite signs to the downgradient mixing phase and K_S and K_T are both negative.

If the flow is unstratified, there is no countergradient phase, and the first of these effects, that is, more effective downgradient transport of S, must prevail, leading to $d = K_S/K_T > 1$ as found in section 3. This scenario is illustrated in the left panel of Fig. 4, where the shaded and unshaded patches represent the initial T and S content of a particular fluid element. In moving uniformly away (on average) from its level of origin, the S content of the parcel remains relatively concentrated and S' relatively large, whereas the T content becomes diffuse and T' relatively small, leading to less effective mixing of T than S.

On the other hand, in the stratified case (right panel of Fig. 4), T and/or S act to restratify the parcel after the initial downgradient phase. This, combined with the greater concentration of S anomalies, leads to relatively effective restratification of S, and thus to $d < 1$ if this effect outweighs the more effective initial downgradient transport of S. This is generally the case in the stratified DNS results reported here.

This qualitative difference between stratified and unstratified turbulence is illustrated in Fig. 5, which shows evolution of S in the xz plane in two such instances. Early evolution (upper and middle panels) is quite similar, as buoyancy has not yet strongly influenced the flow. However, at much later times (lower panels), buoyancy has tended to erase S anomalies and restore initial stratification in the stratified case, whereas in the unstratified case S anomalies remain large until damped by molecular diffusion.

Restratification can be quantified by considering the root-mean-square vertical displacement δz_{rms} of fluid

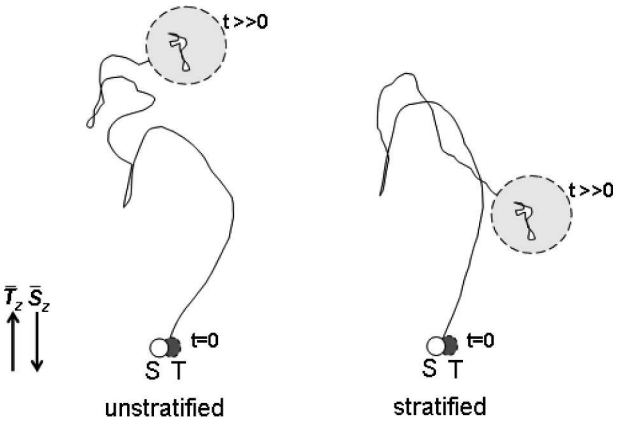

FIG. 4. Schematic of differential mixing by unstratified and stratified turbulence, following evolution of a fluid element whose initial T content is represented by the shaded regions and S content by the unshaded regions. In the unstratified case, mean Lagrangian displacement increases monotonically, and net transport of S exceeds that of the "leakier" component T, leading to $K_S > K_T$. In the stratified case, mean Lagrangian displacement attains a maximum and then decreases as the fluid partially restratifies. The preferential reversal of initial downgradient transport for the more concentrated component S leads to $K_T > K_S$.

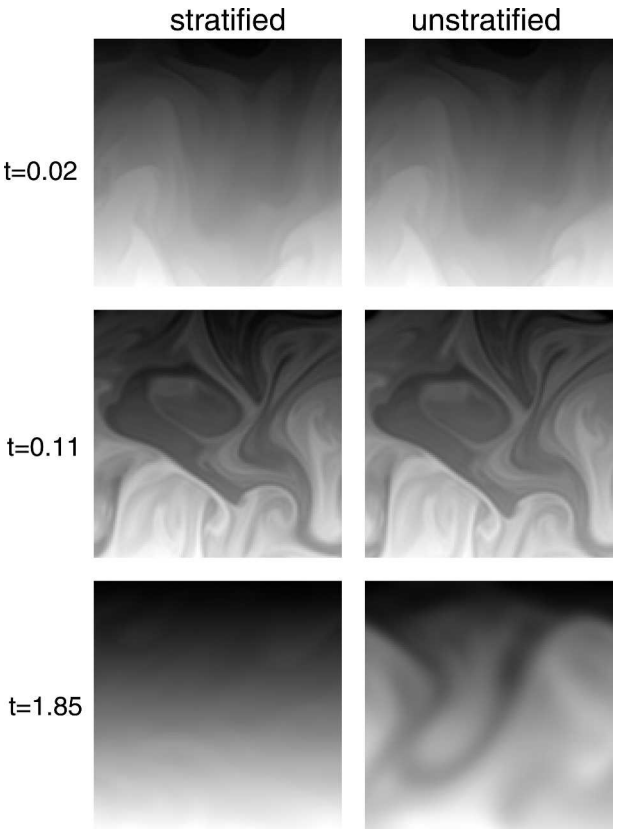

FIG. 5. Evolution of midplane salinity $S(x, y = 0, z)$ for stratified ($N = N_0$, $R_\rho = 1$) and unstratified ($N = 0$) turbulence in high-E_0 case A4.5, at times $t = 0.02$, $t = 0.11$ (time of maximum S variance), and $t = 1.85$.

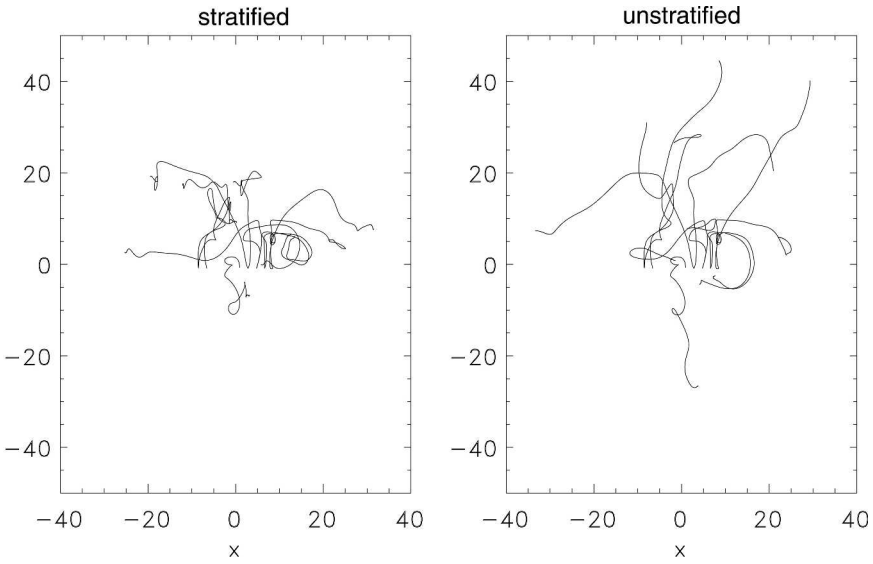

FIG. 6. Trajectories, projected onto the xz plane, of 11 Lagrangian particles initially situated near the x axis whose initial velocities are upward, for stratified ($N = N_0$, $R_\rho = 1$) and unstratified ($N = 0$) turbulence in high-E_0 case A4.5.

particles from their levels of origin. Such displacements were computed in the each of the DNS runs by following the positions of 1000 Lagrangian particles, initially uniformly distributed in space, using fourth-order polynomial interpolation of the velocity field and a Huen time-stepping scheme, as described in Ramsden and Holloway (1991). Figure 6 shows trajectories, projected onto the xz plane, of a number of such particles that initially are situated near the x axis and are moving upward. Vertical dispersion in the (central) stratified case is conspicuously smaller than in the unstratified case, and the tendency for particles in the former instance to be drawn back toward their initial levels is evident. To quantify this tendency, evolving rms vertical displacements for the central and unstratified A4.5 runs are shown in Fig. 7. As discussed above, $\delta z_{\rm rms}$ increases monotonically in the unstratified case, and in the stratified case exhibits a turning point near 1/4 of a buoyancy period $2\pi/N_0$. Because of the diffusive erosion of the S and particularly the T anomalies, the restratification is incomplete.

Based on the above considerations, there should occur a transition with decreasing N between the $d < 1$ and $d > 1$ regimes. Although there is generally (though not uniformly) a tendency for d to increase toward 1 with decreasing N/N_0, such a transition is not realized for the range of N considered here. This perhaps is not surprising, as the quarter-buoyancy period turnaround timescale is at most 2.5 (in units of $2\pi/N_0$) when $N^2/N_0^2 = 0.01$, whereas the diffusive decay time scales are about 6 for T and 60 for the pseudosalinity S. When the buoyancy time scale exceeds the diffusive time scales, values for d should approach those of the unstratified case because little restratification will occur.

b. Dependence on R_ρ

The smaller values of d when T is passive ($R_\rho = 0$) as compared to when S is passive ($R_\rho = \infty$) at fixed N and E_0 can be understood as follows. In the S-passive case (Fig. 8, left), restratification is governed by the more diffusive and hence less concentrated component T, and thus is weaker than when T is passive and restratification is governed by the less diffusive component S (Fig. 8, right). The preferential restratification of S therefore is greater in the latter case, leading to larger net excess of T transport relative to S transport, and hence lower d.

The greater restratification when T is passive than when S is passive is illustrated in Fig. 9, which shows the

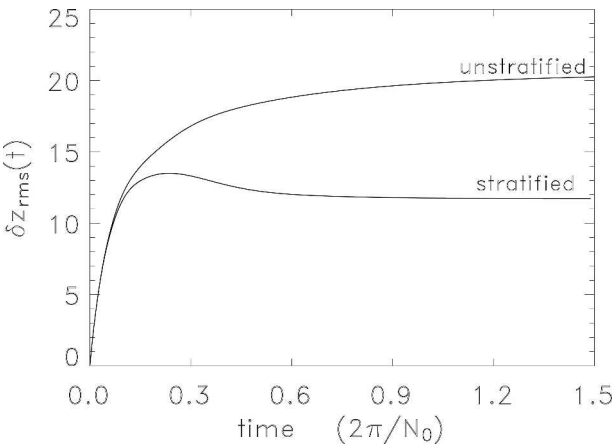

FIG. 7. Evolution of rms vertical displacements of 1000 Lagrangian particles in the central stratified A4.5 run and in the corresponding unstratified run.

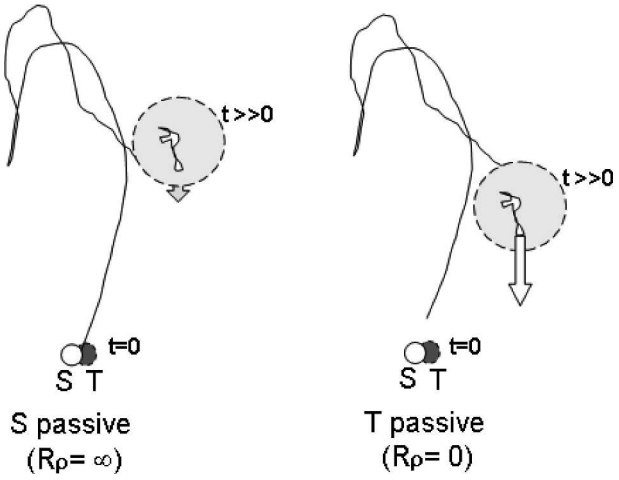

FIG. 8. Schematic as in Fig. 4 of differential mixing when S is passive ($R_\rho = \infty$) compared with when T is passive ($R_\rho = 0$). Restratification (symbolized by the arrows) is more pronounced when T is passive because it is governed by the less diffusive component S. Restratification of S is thus greater, and $d = K_S/K_T$ is smaller, when $R_\rho = 0$ than when $R_\rho = \infty$.

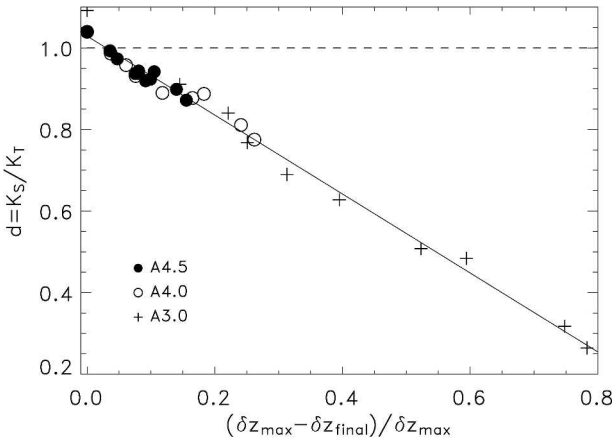

FIG. 10. Turbulent diffusivity ratio d vs fractional restratification $(\delta z_{\max} - \delta z_{\text{final}})/\delta z_{\max}$ for the A4.5, A4.0, and A3.0 runs. The solid line is a linear fit to all the points.

evolving vertical displacements δz_{rms} in these cases for A4.5 with $N = N_0$ and for the $R_\rho = 1$ run shown Fig. 7. In the latter instance, where T and S contribute equally to the background density gradient, the amount of restratification is intermediate. This is reflected in the $R_\rho = 1$ values for d, which also lie between the T-passive and S-passive values (Fig. 2).

c. Differential mixing and restratification

To illustrate further the link between restratification and differential mixing, In Fig. 10 d is plotted against a fractional restratification measure $(\delta z_{\max} - \delta z_{\text{final}})/\delta z_{\max}$, which is 0 for no restratification and 1 when there is complete restratification. All of the $\sigma = 7$ runs for cases A4.5, A4.0, and A3.0 are shown, together with a linear fit to all the points. The tight clustering of the points about the linear fit under a very wide range of N, R_ρ, and initial kinetic energies E_0 is strong evidence for a close connection between restratification and differential mixing.

A further semiquantitative illustration of this connection is provided by the following construct, which models, in a greatly simplified manner, the restratification phase of a turbulent mixing event. The assumptions made are that (i) the Reynolds number during restratification is sufficiently small that the dynamics are linear and are governed solely by buoyancy and dissipation, (ii) Fourier components of T' and S' have zero vertical wavenumber and vary only in the horizontal direction, and (iii) the start of the restratification phase coincides with the turning point of the rms vertical displacement δz so that initial vertical velocities are zero. Of these assumptions, i is somewhat justified, as the Reynolds numbers at the turning points of δz are about 10 or less in all cases, and iii should be justified at least on average. By contrast, assumption ii is made purely for convenience to simplify the calculation. However, because buoyancy and dissipation act similarly in both cases, representing the restratifying fluid elements as columnar rather than as a more isotropic shape should not have a decisive influence. Last, for further simplification we consider only cases in which either T or S is passive so that buoyancy is governed by only one of these components. This is sufficient to bracket behavior over the full range of R_ρ as discussed in section 4b.

Denoting the active tracer ($-T$ or S) by A and the passive tracer by Π, the nondimensional governing equations under these assumptions for a Fourier component with horizontal wavenumber k are

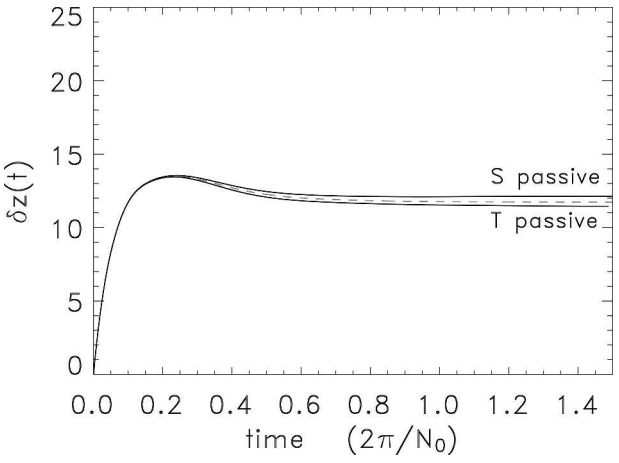

FIG. 9. Evolution of rms vertical displacements of 1000 Lagrangian particles in stratified A4.5, $N = N_0$ runs, when S is passive (top line) and T is passive (bottom line). The intermediate $R_\rho = 1$ case shown in Fig. 5 is indicated by the dashed curve.

$$\frac{\partial w}{\partial t} = -\sigma A - \sigma k^2 w, \tag{7}$$

$$\frac{\partial A}{\partial t} = w - \tau_a k^2 A, \quad \text{and} \tag{8}$$

$$\frac{\partial \Pi}{\partial t} = w - \tau_p k^2 \Pi, \tag{9}$$

where τ_a is the scaled diffusivity for the active tracer (1 for $A = T$ and τ for $A = S$) and τ_p is that for the passive tracer. Initial conditions are

$$w(t_0) = 0, \quad A(t_0) = A_0, \quad \text{and} \quad \Pi(t_0) = \Pi_0, \tag{10}$$

where $t = t_0$ at the turning point of δz.

Because Π does not appear in (7) or (8), the above equations can be solved as a 2×2 eigensystem for w and A, and Π determined afterward using the solution for w.

The eigenvalues of (7)–(8) are

$$\lambda_{\pm} = \frac{k^2}{2}\left[-(\sigma + \tau_a) \pm \sqrt{(\sigma - \tau_a)^2 - 4\sigma k^{-4}}\right] \tag{11}$$

with corresponding eigenvectors (w_+, A_+) and (w_-, A_-), where

$$A_{\pm} = \pm\frac{\lambda_{\mp} + \tau_a k^2}{\lambda_- - \lambda_+} A_0 \quad \text{and} \quad w_{\pm} = (\lambda_{\pm} + \tau_a k^2) A_{\pm}. \tag{12}$$

Evolution of (w, A) for $t \geq t_0$ satisfying initial conditions (10) is given by

$$w(t) = w_+ e^{\lambda_+(t-t_0)} + w_- e^{\lambda_-(t-t_0)} \quad \text{and} \tag{13a}$$

$$A(t) = A_+ e^{\lambda_+(t-t_0)} + A_- e^{\lambda_-(t-t_0)}, \tag{13b}$$

together with (11) and (12).

Because (9) for Π is inhomogeneous, its solution requires combining homogeneous and particular solutions in the usual manner. The result is

$$\Pi(t) = \Pi_+ e^{\lambda_+(t-t_0)} + \Pi_- e^{\lambda_-(t-t_0)} + (\Pi_0 - \Pi_+ - \Pi_-) e^{-\tau_p k^2 (t-t_0)}, \tag{14}$$

with $\Pi_{\pm} = w_{\pm}/(\lambda_{\pm} + \tau_p k^2)$. Given these solutions, it is straightforward to obtain analytically the time-integrated restratifying transports,[4]

$$\mathcal{T}_A = \int_{t_0}^{\infty} w(t) A(t)\, dt \quad \text{and} \quad \mathcal{T}_\Pi = \int_{t_0}^{\infty} w(t) \Pi(t)\, dt. \tag{15}$$

As quantitative measures of the effectiveness of restratifying transport, restratification efficiencies, $\varepsilon_A^{(r)}$ and $\varepsilon_\Pi^{(r)}$, are introduced as the ratios of the actual restratifying transports to the potential restratifying transports, where the latter, defined as the transports that would be achieved by ideal, diffusionless tracers, are both equal to $A_0^2/2$ when the initial active and passive tracer anomalies both have the same magnitude A_0. Thus,

$$\varepsilon_A^{(r)} = \mathcal{T}_A/(A_0^2/2), \varepsilon_\Pi^{(r)} = \mathcal{T}_\Pi/(A_0^2/2). \tag{16}$$

These efficiencies as functions of k are shown in Fig. 11, where the S-passive case ($A = T, \Pi = S$) is considered in the left panel. It is seen that with $\tau = 0.1$ (solid curves), restratifying transport of S exceeds that of T, given equal initial S and T anomalies, by a factor of ~ 2 that depends only weakly on k. Not surprisingly, both efficiencies decrease strongly with increasing k because of the tendency of diffusion to damp the anomalies.

The right panel of Fig. 11 shows restratification efficiencies for the T-passive case ($A = S, \Pi = T$). When $\tau = 0.1$ (solid curves), both efficiencies are larger than in the S-passive case. This is because in this instance restratification is driven by the more weakly diffusing component S (Fig. 8). In addition, the ratio $\varepsilon_S^{(r)}/\varepsilon_T^{(r)}$ is larger than in the S-passive case. Both of these considerations indicate that preferential restratification of S is more pronounced when T is passive than when S is passive.

These results also provide an indication of sensitivity to τ, which is of interest because the realistic value $\tau = 0.01$ is not accessible in the numerical experiments. In Fig. 11, results with $\tau = 0.01$ are indicated by the dashed curves. When S is passive (left), restratification efficiency for S is slightly greater than for $\tau = 0.1$ whereas, predictably, making the passive tracer S less diffusive has no effect on the active tracer T. This relatively low sensitivity of $\varepsilon_S^{(r)}$ to τ can be understood as resulting from the inherent weakness of restratifying motions when T is the restratifying agent; reducing S diffusion in such cases does little to enhance restratification of S. By contrast, when T is passive (right) and S is the restratifying agent, reducing S diffusion substantially increases $\varepsilon_S^{(r)}$ because reduced diffusion of the S anomalies facilitates greater restratification. An implication is that in going from $\tau = 0.1$ to $\tau = 0.01$ we should expect little change in d when R_ρ is large, but significant changes, in the sense of d becoming smaller, when R_ρ is small.

The preceding arguments actually *underestimate* preferential restratification of S over that of T because of the assumption that T and S anomalies are equal when restratification begins. In actuality, S anomalies already exceed T anomalies at this point because of preferential diffusive decay of the latter during the downgradient mixing phase. For example, at the turn-

[4] To further simplify the analysis, it is assumed at this point that k is sufficiently large that gravity waves are overdamped, so that the eigenvalues and eigenvectors are strictly real. This requires $(\sigma - \tau_a)^2 > 4\sigma k^{-4}$, or $k \gtrsim 0.87$ as compared with the fundamental wavenumber 0.33.

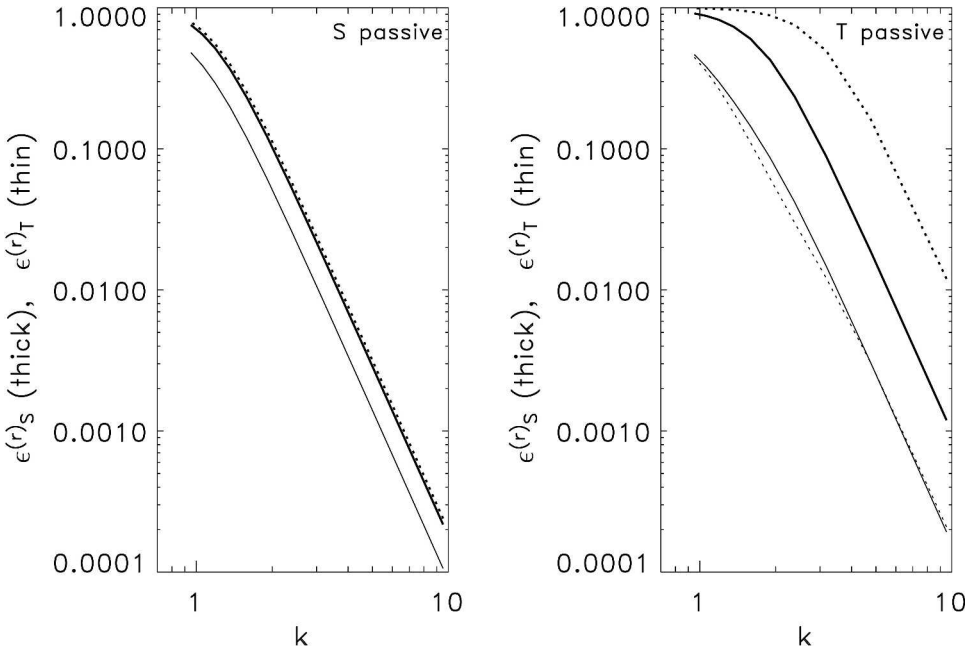

FIG. 11. Restratification efficiencies $\varepsilon_S^{(r)}$ and $\varepsilon_T^{(r)}$, defined as the time-integrated restratifying transports as fractions of those that would be achieved by a diffusionless active tracer, as functions of wavenumber k when (left) S is passive and (right) T is passive. In both panels the thick curves represent restratification efficiencies for S and the thin curves those for T; $\tau = 0.1$ for the solid curves, whereas $\tau = 0.01$ for the dashed curves.

ing point of the central A4.5 experiment, variance of T is about 0.6 times that of S. The actual ratio of restratifying transports will be that obtained when these differences in the initial anomalies, which become more pronounced with increasing k, are taken into account. Figure 12 shows the ratio of restratification transports of T to those of S as functions of k and of the T variance/S variance ratio at $t = t_0$. When this ratio is 1, the plotted values correspond to the ratio of $\varepsilon_T^{(r)}/\varepsilon_S^{(r)}$ of the values in Fig. 11. It is seen that under these more realistic conditions the smallness of the restratifying transports of T in comparison with those of S becomes even more pronounced, as predicted above.

A perhaps unexpected result is that the restratification-phase transports of T are predicted to reverse sign and become downgradient when T is passive and initial T variance is relatively small. The reason for this is as follows. Consider the limit in which T anomalies have decayed to a minute fraction of the S anomalies prior to restratification. As an upward-displaced parcel with positive S' and (nearly vanishing) negative T' begins to sink because of the negative buoyancy due to S', the parcel will acquire positive T' as it sinks to levels where ambient T is lower.

5. Discussion

In this section, results of sections 3 and 4 are discussed in the context of recent laboratory and theoretical investigations concerning the dependence of differential diffusion on various parameters.

a. *Laboratory experiments of Jackson and Rehmann*

In the experiments of Jackson and Rehmann (2003), a fluid stratified by initially uniform stabilizing gradients of heat and salt is stirred continuously by oscillating rods. These experiments provide relatively precise estimates for K_S and K_T over a large range of turbulence intensity as measured by the buoyancy Reynolds number $\varepsilon/\nu N^2$. Although the experiments differ in several respects from the DNS described in this paper, including the use of continuous rather than episodic stirring and $\tau = 0.01$ instead of $\tau = 0.1$, it is of interest to compare the two sets of results. In Fig. 13, the small symbols denote the results reported by JR. As in their Fig. 10, filled symbols designate experiments at relatively low R_ρ ($0.2 \lesssim R_\rho \lesssim 0.3$) and open symbols experiments at relatively high R_ρ ($4 \lesssim R_\rho \lesssim 5$). For the DNS, $\varepsilon/\nu N^2$ is assigned its value at the time of maximum S variance. The large squares represent the values for d reported in section 3, and results for $R_\rho = 0$, 1, and ∞ are represented by dark, gray, and white squares respectively. In addition, the corresponding circles indicate values of d for a diffusionless passive tracer, which can be estimated from the Lagrangian trajectory information as detailed in the appendix. Because $\tau = 0$ for such a tracer, these values and those for $\tau = 0.1$ (large

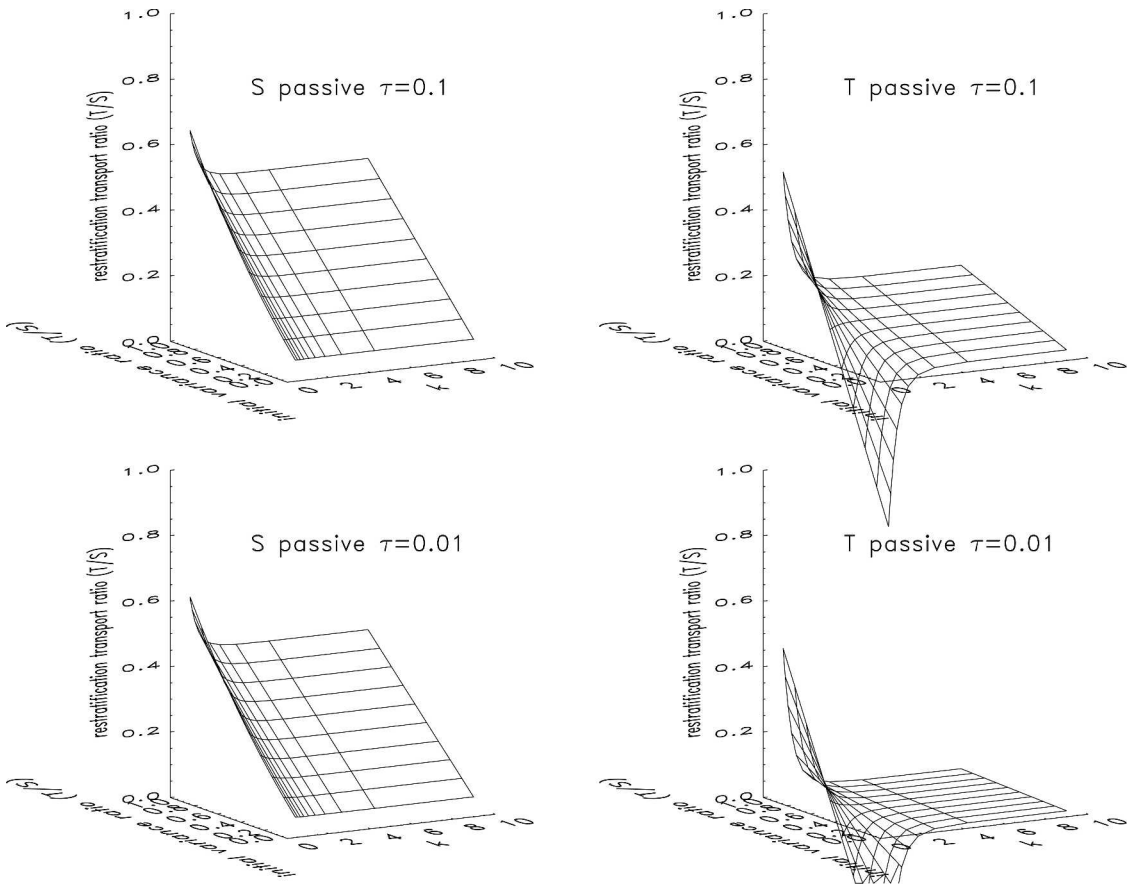

FIG. 12. Ratio of restratifying transport of T to that of S as a function of wavenumber k and the ratio of T variance to S variance at time t_0 when restratification begins.

squares) can be viewed in an approximate sense as bracketing the $\tau = 0.01$ case considered by JR, although of course the diffusionless Lagrangian particles do not contribute to buoyancy.

In examining Fig. 13, several general observations can be made.

1) For both the laboratory and DNS results, d is broadly an increasing function of $\varepsilon/\nu N^2$.
2) Whereas generally $d < 1$ at smaller $\varepsilon/\nu N^2 \lesssim 10^3$, frequently $d > 1$ for $\varepsilon\nu N^2 \gtrsim 10^3$, particularly for the $\tau = 0.01$ laboratory experiments and the $\tau = 0$ particles in the DNS.
3) In the DNS, d for the diffusionless particles exhibits a greater spread of values, both low and high, than d for the $\tau = 0.1$ tracer S, indicating larger differential effects for the less diffusive tracer.
4) Whereas d at given $\varepsilon/\nu N^2$ in the DNS tends to increase with increasing R_ρ (see also Fig. 2), no such trend is evident in the laboratory results.

Overall, the laboratory and DNS results are not glaringly dissimilar, which is perhaps surprising given differences between the continuous mixing in the laboratory experiments and the episodic mixing in the DNS. In particular, the role of restratification under continuous mixing is likely more subtle, perhaps involving simultaneous downgradient fluxes in one wavenumber range and upgradient fluxes in another, as discussed in GMH sections 5a and 6.

b. Laboratory experiments of Hebert and Ruddick

The laboratory experiments of Hebert and Ruddick (2003) differ from those of JR in several important respects. First, the fluid is mixed intermittently by breaking internal waves rather than being continuously stirred, and so the HR experiments are perhaps closer phenomenologically to the DNS than the JR experiments. A second difference is that the HR experiments examine differential mixing between two dyes having different molecular diffusivities, rather than between heat and salt. A third difference is that, in all but two of the HR experiments, buoyancy is provided solely by salt so that the two dyes (whose molecular diffusivities both exceed that of salt) are passive tracers. In the remaining experiments, buoyancy is provided in equal parts by salt and the slower-diffusing dye. Last, the Prandtl number, defined as the ratio of viscosity to molecular diffusivity of the fastest-diffusing component, is

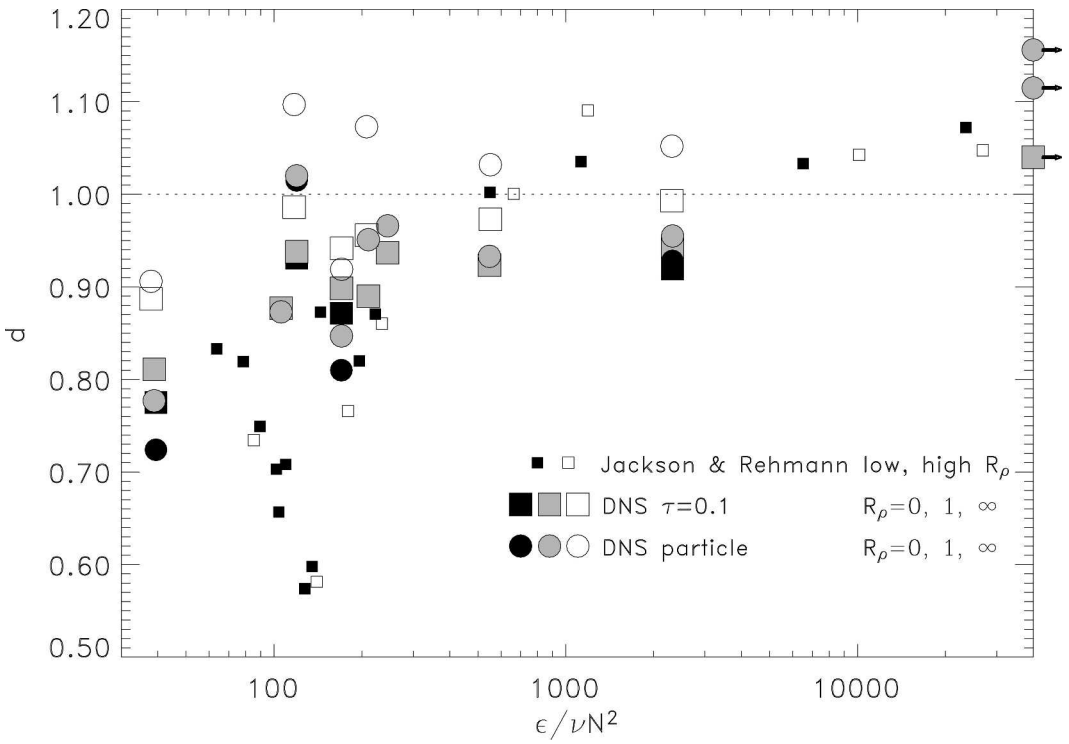

FIG. 13. Measurements of d vs buoyancy Reynolds number $\varepsilon/\nu N^2$ from laboratory experiments of Jackson and Rehmann (2003), in which fluid stabilized by temperature and salinity ($\tau = 0.01$) gradients is continuously stirred, and from the A4.5 and A4.0 DNS runs. In the DNS, $\varepsilon/\nu N^2$ is calculated at the time of maximum S variance, and values of d are indicated both for when the less diffusive component is S ($\tau = 0.1$) and when it is a diffusionless ($\tau = 0$) passive tracer as estimated from Lagrangian particle trajectories (see the appendix). The points at the right-hand edge are for unstratified turbulence, for which $\varepsilon/\nu N^2 \to \infty$. Error bars for the Jackson and Rehmann measurements, provided in their Fig. 8, are small relative to the scatter.

much larger in the HR experiments than the $O(10)$ values characterizing the JR experiments and the DNS.

Despite these differences, the experimental results, shown in HR Fig. 2, are strikingly similar to those of JR and to the present DNS. In particular, d, defined by HR as the ratio of the turbulent diffusivity of the slower-diffusing dye to that of the faster-diffusing dye, increases from ~0.7 to values significantly exceeding unity as $\varepsilon/\nu N^2$ increases over two or so orders of magnitude, although the estimated values of $\varepsilon/\nu N^2$ over which the transition takes place are $O(10^4)$ times less than for JR or the present DNS. This difference may in part be due to the relatively large Prandtl number in the HR experiments, which for given $\varepsilon/\nu N^2$ should lead to greater restratification, and hence differential mixing, than in the heat/salt case, particularly when the faster-diffusing component provides stratification. Such a tendency is evident in comparing the $R_\rho = \infty$ results for the default A4.0 simulations having $\sigma = 7$ with the corresponding $\sigma = 2$ results in Fig. 2.

An additional aspect of the HR results that bears mention is that in the experiments where the slower diffusing dye is an active tracer, d is slightly smaller than in experiments where both dyes are passive. This is consistent with the description of restratification effects developed in section 4 and with the DNS results: when buoyancy is provided the slower-diffusing dye, restratification should be more pronounced than when buoyancy is provided solely by relatively diffusive salt. The less diffusive tracer should thus restratify more effectively in the former case, and d should be smaller, as is observed.

c. *Closure theory of Canuto et al.*

In Canuto et al. (2002), a third-order closure approximation is applied to equations describing evolution of second-order moments of **u,** T, and S under the influence of ocean turbulence. Predicted $d = K_S/K_T$ as functions of R_ρ and Richardson number Ri^T are shown in their Fig. 5c, where it is assumed that turbulence is steady, Reynolds number is high, and energy is supplied by shear so that turbulence does not exist above a critical value of Ri^T. These results predict that d increases with increasing R_ρ,[5] and that the range over which d varies with R_ρ diminishes as Ri^T decreases and turbu-

[5] Bear in mind that Canuto et al. (2002) define $R_\rho = \beta\overline{S}_z/\alpha\overline{T}_z$, whereas $R_\rho = -\alpha\overline{T}_z/\beta\overline{S}_z$ here.

lence becomes more energetic. Both these tendencies are in qualitative agreement with the DNS reported in Fig. 2. The result of Canuto et al. (2002) that $d = 1$ when $R_\rho = 1$ and $d > 1$ when $R_\rho > 1$ differs from the results presented here, but is a consequence of particular closure relations, for example, their (21a) and (22d), that are specific to high Reynolds numbers in contrast to the relatively low Reynolds numbers considered here.

6. Conclusions

This paper has extended the study of Gargett et al. (2003) to consider dependence of differential mixing on stratification parameters N and R_ρ in DNS experiments representing mixing by a burst of turbulence. In contrast to the preferential mixing of temperature, ($d = K_S/K_T < 1$) found by Gargett et al. when $N = N_0$ and $R_\rho = 1$, here it is found that S can be mixed more effectively than T ($d > 1$) when the fluid is unstratified ($N = 0$). By extension, it is expected that a transition from $d < 1$ to $d > 1$ will occur when N is sufficiently small or turbulence is sufficiently intense that the influence of buoyancy becomes relatively unimportant.

In considering dependence on R_ρ, it was found that d uniformly increases with increasing R_ρ when other parameters are fixed. In particular, in the limit where T is passive and buoyancy is provided solely by S ($R_\rho \to 0$), d is always less than in the opposite limit where S is passive and buoyancy is provided solely by T ($R_\rho \to \infty$). As discussed in section 4, this can be understood if $d < 1$ is viewed as being due to preferential restratification of the less diffusive and therefore more concentrated component *S:* when T is passive restratification is relatively strong, whereas when S is passive restratification is effected by the more diffuse component T and is thus relatively weak, leading to larger d. This phenomenon was illustrated by a simple semiquantitative construct in section 4.

The strong link between restratification and differential mixing is especially clear in Fig. 10, which shows that a nearly linear relationship exists between d and a fractional restratification index over a wide range of conditions.

Several aspects of the DNS results, including (i) the tendency for d to increase with buoyancy Reynolds number $\varepsilon/\nu N^2$ and (ii) the possibility for $d > 1$ at sufficiently high $\varepsilon/\nu N^2$, were shown to be consistent with laboratory experiments of Jackson and Rehmann (2003) and Hebert and Ruddick (2003), even though the properties of the diffusing scalars and of the mixing itself differed between the two experiments and the DNS. Similarly, the tendency for d to increase with increasing R_ρ is consistent with predictions of the closure theory of Canuto et al. (2002).

As in other investigations of differential mixing, the DNS described here do not exactly replicate the conditions under which such mixing occurs in the ocean. In particular, the molecular diffusivity of the more slowly diffusing scalar S is 0.1 times that of T, whereas for true salinity this ratio is closer to 0.01. The present results therefore underestimate differential mixing effects. In addition, the DNS mixing scenario, consisting of a single turbulent burst generated by an imposed initial velocity field, differs from mixing in the ocean, where turbulent kinetic energy is generated by dynamical instabilities that recur intermittently rather than being completely isolated in time. Differential diffusion arising from shear instability has recently been examined by Smyth et al. (2005, this issue), who find a dependence of d on $\varepsilon/\nu N^2$ and R_ρ consistent with that reported here.

Acknowledgments. Impetus for this work was provided by discussions with Greg Holloway and Ann Gargett, and by the efforts of Chris Rehmann and Dave Hebert to organize a special session on differential mixing at the 2004 ASLO/TOS Ocean Research Conference. Chris Rehmann and Ryan Jackson kindly provided experimental data depicted in Fig. 13. Bill Smyth, Vittorio Canuto, John Scinocca, Charles Curry, and an anonymous reviewer are thanked for helpful comments and suggestions.

APPENDIX

Eulerian Diffusivities from Lagrangian Particle Dispersion

In each of the DNS the positions of $M = 1000$ Lagrangian particles, initially equally spaced, are computed. It is shown here that this information can be used to estimate a turbulent diffusivity ratio $\tilde{d} = K_R/K_T$, where R is equivalent to a diffusionless, passive tracer having uniform background gradient $\overline{R}_z$. These estimates of $\tilde{d}$ are discussed in section 5a and are displayed as round symbols in Fig. 13.

Consider first the vertical displacement of each particle from its initial level. Denoting such displacements by $\delta z_i(t)$ ($i = 1, \ldots, M$), the vertical particle velocities can be expressed as $w_i = \delta \dot{z}_i$. Because tracer R is diffusionless, the tracer anomaly associated with particle i is $R_i' = \overline{R}_z \delta z_i$. An estimate of the spatially averaged vertical flux of R, sampled at the particle locations, is

$$\langle wR' \rangle \approx M^{-1} \sum_{i=1}^{M} w_i \delta z_i \overline{R}_z, \tag{A1}$$

and the temporally integrated transport from $t = 0$ to $t = t_{\max}$ is

$$\int_0^{t_{\max}} \langle wR' \rangle \, dt \approx \frac{1}{2} \langle \delta z^2 \rangle_{t_{\max}} \overline{R}_z, \tag{A2}$$

where $\langle \delta z^2 \rangle$ is the variance of vertical Lagrangian displacement. Scaling by the ambient gradient and divid-

ing by integrated transport of T as in (7) provides the desired estimates of $\tilde{d}$.

REFERENCES

Altman, D. B., and A. E. Gargett, 1990: Differential property transport due to incomplete mixing in a stratified fluid. *Stratified Flows,* E. J. List and G. H. Jirka, Eds., American Society of Civil Engineers, 454–460.

Batchelor, G. K., 1959: Small scale variation of convected quantities like temperature in a turbulent fluid. *J. Fluid Mech.,* **5,** 113–133.

Canuto, V. M., A. Howard, Y. Cheng, and M. S. Dubovikov, 2002: Ocean turbulence. Part II: Vertical diffusivities of momentum, heat, salt, mass and passive scalars. *J. Phys. Oceanogr.,* **32,** 240–264.

Gargett, A., 2003: Differential diffusion: An oceanographic primer. *Progress in Oceanography*, Vol. 56, Pergamon, 559–570.

——, and G. Holloway, 1992: Sensitivity of the GFDL ocean model to different diffusivities for heat and salt. *J. Phys. Oceanogr.,* **22,** 1158–1177.

——, W. J. Merryfield, and G. Holloway, 2003: Direct numerical simulation of differential scalar diffusion in three-dimensional stratified turbulence. *J. Phys. Oceanogr.,* **33,** 1758–1782.

Hebert, D., and B. R. Ruddick, 2003: Differential mixing by breaking internal waves. *Geophys. Res. Lett.,* **30,** 1042, doi:10.1029/2002GL016250.

Jackson, P. R., and C. R. Rehmann, 2003: Laboratory measurements of differential diffusion in a diffusively stable, turbulent flow. *J. Phys. Oceanogr.,* **33,** 1592–1603.

Merryfield, W. J., G. Holloway, and A. E. Gargett, 1998: Differential vertical transport of heat and salt by weak stratified turbulence. *Geophys. Res. Lett.,* **25,** 2773–2776.

——, ——, and ——, 1999: A global ocean model with double-diffusive mixing. *J. Phys. Oceanogr.,* **29,** 1124–1142.

Nash, J. D., and J. N. Moum, 2002: Microstructure estimates of turbulent salinity flux and the dissipation spectrum of salinity. *J. Phys. Oceanogr.,* **32,** 2312–2333.

Ramsden, D., and G. Holloway, 1991: Timestepping Lagrangian particles in two-dimensional Eulerian flow fields. *J. Comput. Phys.,* **95,** 101–116.

Smyth, W. D., J. D. Nash, and J. N. Moum, 2005: Differential diffusion in breaking Kelvin–Helmholtz billows. *J. Phys. Oceanogr.,* **35,** 1004–1022.

Turner, J. S., 1968: The influence of molecular diffusivity on turbulent entrainment across a density interface. *J. Fluid Mech.,* **33,** 639–656.